INTERNATIONAL JOURNAL OF HYDROGEN ENERGY 45 (2020) 12982–12996

Available online at www.sciencedirect.com
ScienceDirect
journal homepage: www.elsevier.com/locate/he

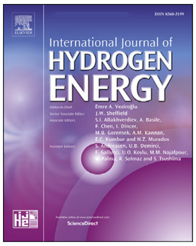

Structural and catalytic properties of ceria layers doped with transition metals for SOFCs fueled by biogas

B. Hołówko [a], P. Błaszczak [b], M. Chlipała [c], M. Gazda [b], S.-F. Wang [d], P. Jasiński [a], B. Bochentyn [b,*]

[a] Faculty of Electronics, Telecommunications and Informatics, Gdansk University of Technology, 80-233, Gdansk, Ul. Narutowicza 11/12, Poland
[b] Faculty of Applied Physics and Mathematics, Gdansk University of Technology, 80-233, Gdansk, Ul. Narutowicza 11/12, Poland
[c] Institute of High Pressure Physics, Polish Academy of Sciences, 01-142, Warszawa, Ul. Sokołowska 29/37, Poland
[d] Department of Material and Mineral Resources Engineering, National Taipei University of Technology, 1, Sec. 3, Zhongxiao E. Rd., Taipei, 106, Taiwan

HIGHLIGHTS

- $Ce_{0.8}A_{0.2}O_{2-\delta}$ (A = Mn, Fe, Co, Ni, Cu) was synthesized by reverse microemulsion method.
- Fourier Transformed Infrared Spectroscopy was used to analyze a composition of outlet gases.
- $Ce_{0.8}Co_{0.2}O_{2-\delta}$ and $Ce_{0.8}Ni_{0.2}O_{2-\delta}$ additional layers were the most stable in time.

GRAPHICAL ABSTRACT

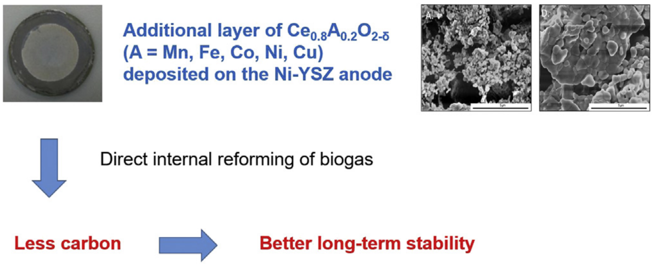

ARTICLE INFO

Article history:
Received 19 October 2019
Received in revised form
15 February 2020
Accepted 21 February 2020
Available online 30 March 2020

Keywords:
Biogas
Reforming

ABSTRACT

The aim of this paper was to investigate an influence of the nanocrystalline $Ce_{0.8}A_{0.2}O_{2-\delta}$ (A = Mn, Fe, Co, Ni, Cu) materials on the direct internal reforming of biogas in SOFC. Structural analysis of fabricated compounds has been done. An in-situ analysis of a composition of outlet gases from operating SOFC was performed using FTIR spectroscopy with simultaneous electrical tests. It was found out, that type of dopant strongly affects biogas reforming process. The differences in absolute values of current density resulted mostly from a microstructure and probably phase composition of a deposited layers. Fuel cells with $Ce_{0.8}Co_{0.2}O_{2-\delta}$ and $Ce_{0.8}Ni_{0.2}O_{2-\delta}$ additional layers presented the highest drop of current density after switching from hydrogen to biogas, but simultaneously they were the most stable in time. Additional chemical analysis revealed that

---

* *Corresponding author.*
E-mail address: beata.bochentyn@pg.edu.pl (B. Bochentyn).

https://doi.org/10.1016/j.ijhydene.2020.02.144

Ceria
Transition metal
Reaction quotient

steam reforming and methane pyrolysis might be dominating reactions while working in biogas atmosphere.

Introduction

Nowadays alternative and green energy sources draw a lot of researchers' attention. One of many devices that allows obtaining energy without emitting as much pollutants as conventional systems is a Solid Oxide Fuel Cell (SOFC) [1]. It consists of three main elements. A cathode, called an oxygen electrode, an anode, called a fuel electrode and an electrolyte. The most common material used for SOFC anodes is a ceramic composite made of yttria stabilized zirconia mixed with nickel (Ni-YSZ). This material is cheap, easily available and has good catalytic properties for hydrogen oxidation.

While concerning SOFC technology for energy production, a big advantage is that diverse gaseous fuels can be utilized. SOFCs work with the highest efficiency if pure hydrogen is being used. However, high production cost as well as difficulties in storage and transportation of hydrogen causes other substances to be more likely used as a fuel to power-up fuel cells. The most interesting from practical point of view are pure methane and products obtained from fermentation of organic compounds, i.e. biogas. The biogas composition may vary but most commonly it is a mixture of methane and carbon dioxide. Additionally, traces of water, nitrogen and sulfur compounds may also be present [2–8].

In order to use a mixture of hydrocarbons or biogas as a fuel, the gas must undergo so called reforming process, which results in hydrogen formation. Further, obtained hydrogen is being used up by operating cell. Mentioned process can be carried out either externally, outside the system or internally, using anode's surface. In more advanced SOFCs systems, the use of internal reforming using the catalytic activity of the anode is more desirable. General chemical reactions occurring during biogas reforming are shown in Eqs. (1)–(7) [9].

$$CH_4 + CO_2 \leftrightarrow 2CO + 2H_2 \tag{1}$$

$$CH_4 + H_2O \leftrightarrow CO + 3H_2 \tag{2}$$

$$CO_2 + H_2 \leftrightarrow CO + H_2O \tag{3}$$

$$CO_2 + 4H_2 \leftrightarrow CH_4 + 2H_2O \tag{4}$$

$$CH_4 \leftrightarrow C + 2H_2 \tag{5}$$

$$2CO \leftrightarrow C + CO_2 \tag{6}$$

$$CO + H_2 \leftrightarrow C + H_2O \tag{7}$$

Moreover, the electrochemical reactions with the oxygen ions passing through the electrolyte should be taken into account:

$$H_2 + O^{2-} \leftrightarrow H_2O + 2e^- \tag{8}$$

$$CO + O^{2-} \leftrightarrow CO_2 + 2e^- \tag{9}$$

$$CH_4 + O^{2-} \leftrightarrow 2H_2 + CO + 2e^- \tag{10}$$

$$C_{solid} + O^{2-} \leftrightarrow CO + 2e^- \tag{11}$$

Although reforming process is commonly known, kinetics and exact intermediate steps of whole process are still under consideration. Basically, hydrogen and carbon monoxide are formed as a result of the reforming processes (Eq. (1) and (2)). It should be also noted, that simultaneously with the main reactions other processes occur. Among them reactions presented as Eqs. (5)-(7) are particularly undesired, as they can lead to the deactivation of anode's catalytic material and to the deterioration of the whole fuel cell performance by a solid carbon accumulation.

Therefore, the use of Solid Oxide Fuel Cells directly fed by the biogas is associated with some technical issues. A traditional fuel cell electrode material, Ni-YSZ, suffers from two main problems while operating with fuels other than pure hydrogen. The first one is a poisoning phenomenon, consequently destroying the anode's surface by formation of sulfur, chloride or phosphorus compounds of nickel, which are rather chemically inactive when it comes to breaking H–H and C–H bonds [10,11]. On the other hand, deposition of different carbon species also causes degradation and a decrease in overall performance via lowering active surface for adsorption of reacting species [12]. Over the years, numerous studies have been performed, both theoretical and practical, regarding this issue [13–17]. One of the possibilities in order to improve the performance of SOFC is to use alternative materials for electrodes, what was also investigated by our group [18–22]. Another solution is to look for an additional improvement of widely tested systems. Additional catalytic layer applied to the anode side should improve the efficiency and stability of the fuel cell. Ceria-based materials were reported as potentially good catalytic compounds for an internal biogas reforming. Due to a high oxygen capacity and ion mobility they are able to prevent coking and thus to improve a long-term stability of the fuel cell [9].

In this work $CeO_{2-\delta}$ doped with transition metals such as Mn, Fe, Co, Ni and Cu as well as a reference non-doped material were fabricated and studied. These materials were used as an additional catalytic layers deposited on the surface of SOFC's anode in order to prevent a fast degradation process of the fuel cell resulting mainly from a deposition of carbon. The influence of particular catalytic layers on the SOFC performance as well as on the direct internal reforming of biogas was systematically analyzed and compared basing on the original approach (simultaneous measurements of electrical parameters and analysis of outlet gases from SOFC) that was described in details in our previous paper [23]. For comparison the results obtained for an unmodified fuel cell (without any catalytic layer) can be also found in paper [23].

Experimental

Material preparation

Cerium oxide doped with transition metals $Ce_{0.8}A_{0.2}O_{2-\delta}$ (where A = Mn, Fe, Co, Ni, Cu) as well as undoped $CeO_{2-\delta}$ were synthesized by the reverse microemulsion method. At the beginning a mixture of pure cyclohexane, pentan-1-ol and nonionic surfactant Triton X-100 was prepared (9.6:1.4:1 by vol.). The appropriate amounts of metal nitrates were dissolved in water in a separate vessel. Both phases were separately stirred for 30 min and then the aqueous phase was added to the organic phase and again stirred for 30 min. After that precipitating agent in the form of tetraethylammonium hydroxide was added. Obtained precipitate was immediately isolated by decantation. The material was then centrifuged and rinsed twice with acetone and methanol. After drying, material was treated at 500 °C for 2 h in air to remove residual organic phase and decompose nitrates.

Catalytic layer fabrication

The anode-supported SOFC was fabricated as described in other paper [24]. The anode (thickness 440 μm) composed of NiO-YSZ had two levels of porosity (with and without a performer). The electrolyte (thickness 10 μm) was YSZ and the cathode was LSM-YSZ composite (thickness 30 μm, surface area of 1.13 cm^2). The ESL 403 organic binder was added to the fabricated ceria-based powders and then mixed to form a uniform paste. The screen-printing method was used to deposit a catalytic layer on the anode side. After drying at 100 °C, layers were sintered at 1000 °C for 2 h.

Measurement techniques

The X-Ray diffraction (XRD) was used to determine the phase composition and to estimate size of crystallites of the fabricated material. The XRD measurements were performed using X'Pert Pro MPD Philips diffractometer using Cu Kα (λ = 1.542 Å) radiation at room temperature. The Scanning Electron Microscope (SEM, FEI Quanta FEG 250) with the energy-dispersive X-ray spectroscope (EDX, EDAX Genesis APEX 2i) and Apollo X SDD detector operating at 10 kV were used to study the morphology and composition of powders. The measurements of SOFC operating parameters together with the analysis of the outlet gases composition were performed by a dedicated system described in details in our previous work [23]. A composition of outlet gases was determined on the basis of FTIR measurements. Both CH_4, CO_2 and CO gases were analyzed. Due to fact that H_2 is not visible in FTIR spectra, after a calibration process it was possible to determine its concentration by simple subtraction. Such an approach is in line with expectations. In order to form a synthetic biogas both CH_4 and CO_2 were supplied in a 3:2 ratio by vol. with a total flow rate of the gas mixture equal to 40 $cm^3 min^{-1}$. A gas humidifier allowed to add 3% of water into the flowing gas. A fuel cell mounted in a measuring rig was put into the tubular furnace and heated up to 800 °C in argon atmosphere and then the gas was switched to hydrogen to perform anode's reduction for 30 min. After initial reduction, the temperature was decreased to 750 °C and electrical measurements were taken at this temperature. After 18 h of operation in hydrogen the fuel was switched to synthetic biogas and the analysis was continued for 90 h. Two types of data from electrical measurements were collected, a current density versus voltage and a current density versus time at static load of 0.65 V. During these measurements the composition of anode outlet gas was simultaneously analyzed by the FTIR spectrometer. According to procedure described in our previous work [23], using concentrations of outlet gases, parameters describing general performance of fuel cells were calculated. Those are CH_4 and CO_2 conversion rates, CO and H_2 yields as well as CO and H_2 selectivities.

Chemical non-equilibrium analysis of reforming reactions' direction

In order to determine a behavior of reactions given in Eqs. (1)–(7) an additional analysis of non-equilibrium state was performed based on a composition of exhaust gases at following measuring points. Exact procedure of data processing and detailed calculation scheme were presented in our previous work [23]. A direction of each reaction can be predicted according to obtained values of Q_r. To examine thermodynamic possibility of solid carbon formation caused by reactions noted in Eqs. (5)–(7), the carbon activity coefficients were calculated as a Q_r reciprocals [23].

Results and discussion

XRD

The XRD patterns of fabricated powders are presented in Fig. 1. It can be said, that all of them, except cobalt-doped cerium oxide, are single phase materials. In the case of $Ce_{0.8}Co_{0.2}O_{2-\delta}$ sample, a small peak appeared at around 36.5°, which can be attributed to the Co_3O_4 phase. The peak is visible in the inset of Fig. 1. The solubility limits in ceria obtained from the literature for the particular elements are as follows: Mn 3% [25], Fe 10% [26], Co 3% [27], Ni 10–33,3% [28] and Cu 15% [29]. This may indicate, that the solubility limit was exceeded and thus a slight amount of additional phase was found in the $Ce_{0\cdot 8}Co_{0\cdot 2}O_{2-\delta}$. However, it should be underlined that solubility limits found in the literature are related to ceria-based compounds obtained using other, than in this paper, synthesis methods and conditions. Moreover, a formation of nanocrystalline instead of microcrystalline material may change the solubility limit by even one order of magnitude [30].

An average size of crystallites was estimated using Scherrer's equation. A mean size of crystallites for a pure ceria was calculated to be around 10 nm, whereas for other doped-ceria compounds it did not exceeded 7 nm.

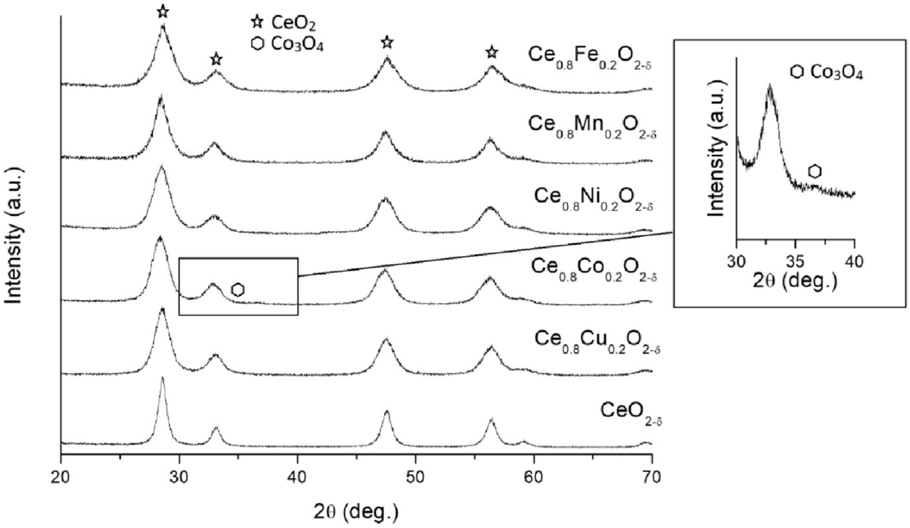

Fig. 1 – XRD patterns of $Ce_{0.8}A_{0.2}O_{2-\delta}$ (where A = Mn, Fe, Co, Ni, Cu) and $CeO_{2-\delta}$.

Microstructure and composition

The grain size of the $Ce_{0.8}A_{0.2}O_{2-\delta}$ and $CeO_{2-\delta}$ powders estimated on the basis of SEM analysis was below 30 nm. However, after materials' deposition in the form of layers followed by sintering at 1000 °C for 2 h a grain coarsening was observed. The microstructure of the surface of the investigated catalytic layers deposited on the SOFC anode before reduction is shown in Fig. 2. The grains have various shapes and sizes. Their size differs depending on a dopant type. The largest grains have been observed for a material with Cu as a dopant, while the smallest for Ni. This indicates a different kinetics of grain growth and agglomeration during the process of layer sintering on the anode's surface. In addition, there is a difference in the porosity of individual materials. The largest pores occurred for the reference catalytic layer and similar for Mn- and Fe-doped ceria. Other materials showed lower porosity. All layers cracked with various intensities, what most probably came from burning out of a binder. The most visible cracks were found in $Ce_{0.8}Cu_{0.2}O_{2-\delta}$ and $CeO_{2-\delta}$ layers.

Additionally, using EDX, the approximate atomic composition was determined for all fabricated ceria-based layers. The results are shown in Table 1. If one takes into account the

Table 1 – Atomic composition of fabricated catalytic layers determined from EDX area analysis.

Nominal composition	Atomic %		
	Cerium	Metal dopant	
$Ce_{0.8}Mn_{0.2}O_{2-\delta}$	79.8%	Mn	20.2%
$Ce_{0.8}Fe_{0.2}O_{2-\delta}$	83.1%	Fe	16.9%
$Ce_{0.8}Ni_{0.2}O_{2-\delta}$	82.0%	Ni	18.0%
$Ce_{0.8}Co_{0.2}O_{2-\delta}$	77.2%	Co	22.8%
$Ce_{0.8}Cu_{0.2}O_{2-\delta}$	89.4%	Cu	10.6%

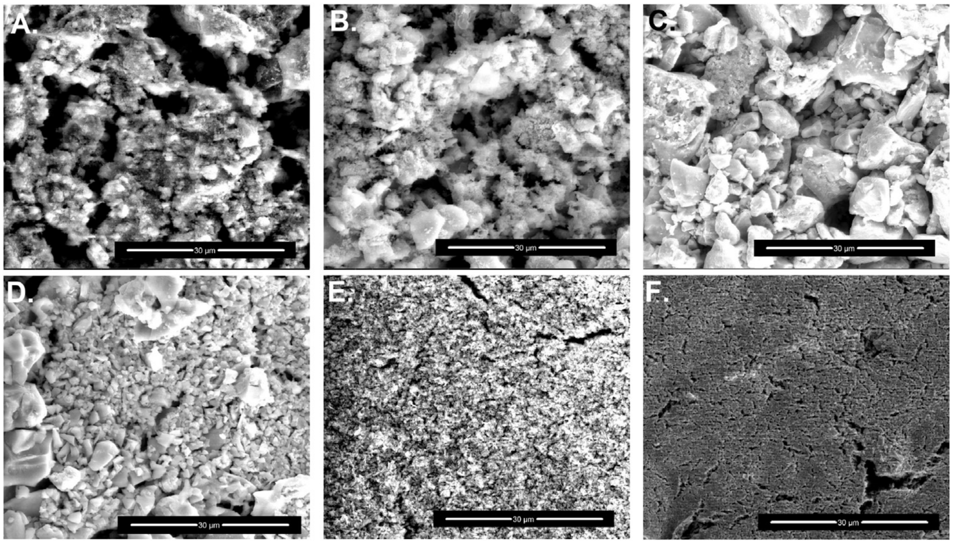

Fig. 2 – SEM micrographs of catalytic layers deposited on the SOFC anode before reduction: undoped CeO_2 (A) and $Ce_{0.8}A_{0.2}O_{2-\delta}$ (doped with Mn (B), Fe (C), Co (D), Ni (E) and Cu (F).

uncertainty of EDX measurement for particular elements (even up to few %), the obtained compositions are close to the assumed nominal stoichiometry described as $Ce_{0.8}A_{0.2}O_{2-\delta}$ (where A = Mn, Fe, Co, Ni, Cu). Only the copper-doped ceria contains twice lower amount of dopant than expected ($Ce_{0.89}Cu_{0.11}O_{2-\delta}$). This depletion may result from the diffusion of copper into the nickel cermet structure or a possible evaporation during sintering.

Electrical tests

I–V plots presented in Fig. 3 have been collected at three different stages of the experiment. The first (initial) and the second (final) correspond to the cell working in hydrogen atmosphere. The first one was taken at the very beginning of the test, whereas the second one after 18 h just before a change of fuel to the synthetic biogas. The third measurement (final in biogas) is related to cells working in the biogas for 90 h. In the case of undoped ceria for the cell working in hydrogen, no decrease in power density is observed. Switching to biogas results in less than 10% decrease of power density. The maximum power density observed for this material in hydrogen (initial) and the synthetic biogas atmosphere is equal to 0.220 and 0.199 W/cm^2, respectively. Fuel cells with additional catalytic layers in the form of ceria doped with Mn, Fe, Co and Cu show a significant decrease of power density in the hydrogen as well as in the biogas atmosphere. This is caused most likely by a degradation of the fuel cell due to a deposition of carbon on the surface. The maximum power densities obtained in hydrogen (initial) and synthetic biogas are equal to 0.228/0.190, 0.232/0.194, 0.238/0.164, 0.227/0.154 W/cm^2 for Mn, Fe, Co and Cu dopants respectively. Only the fuel cell with a Ni-containing catalytic layer shows no change in power density over the entire test. This demonstrates a possible inhibition of degradation process due to the high catalytic activity of nickel. The highest observed power

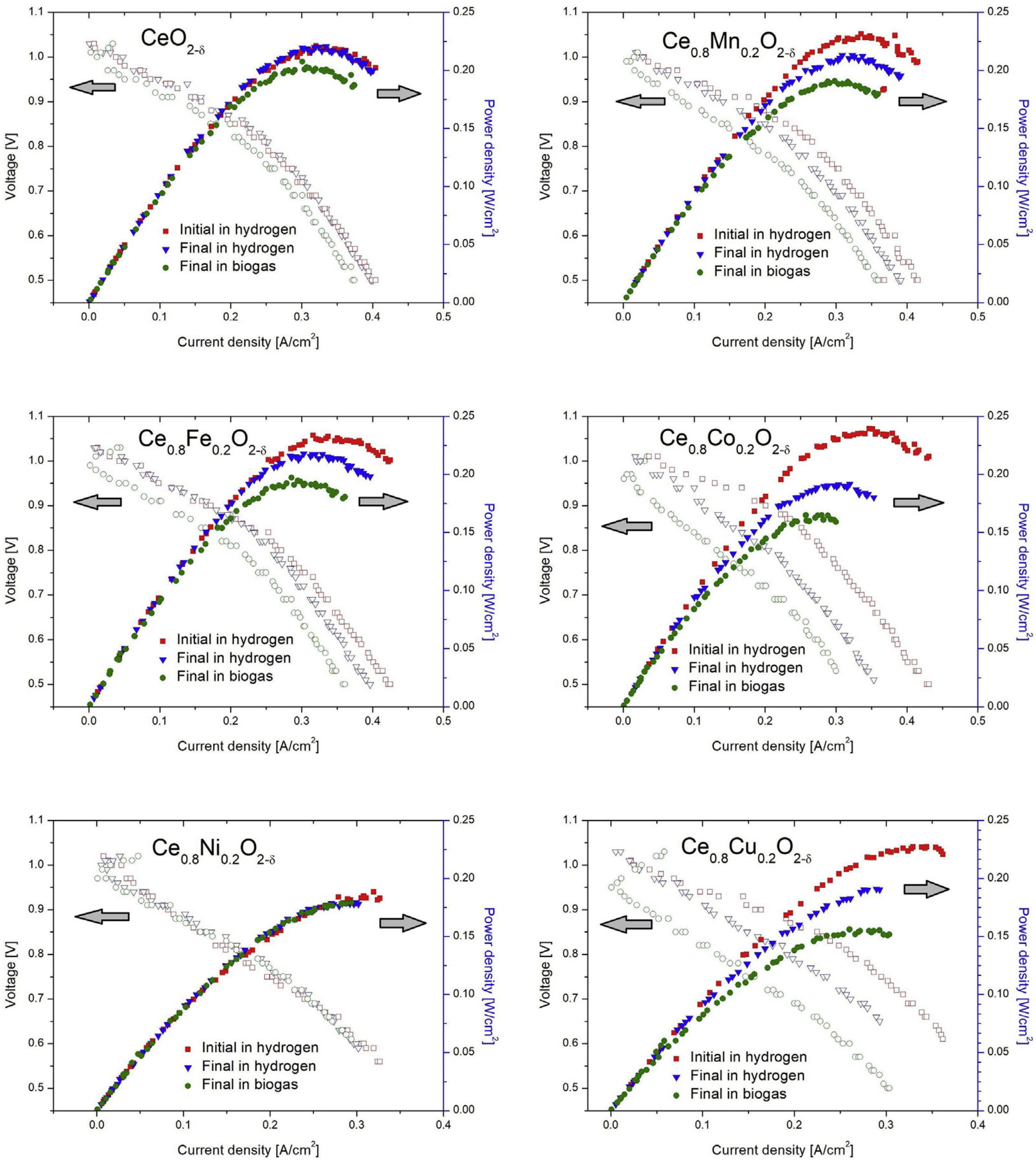

Fig. 3 – The current-voltage and current-power plots for fuel cells with catalytic layers of undoped CeO_2 and $Ce_{0.8}A_{0.2}O_{2-\delta}$ (where A = Mn, Fe, Co, Ni, Cu).

density for the fuel cell with $Ce_{0.8}Ni_{0.2}O_{2-\delta}$ catalytic layer is equal to 0.181 W/cm^2. Such a positive effect in electrical stabilization of SOFC with metal-doped ceria anode was also reported in the literature for W–Ni–CeO_2 [31,32] and Rh/Cu–Ca–CeO_2 [33].

Fig. 4 presents a comparison of a current densities for all investigated fuel cells. Both sets of current density values measured in hydrogen (negative time values) as well as in the biogas have been shown. The absolute change of the current density after switching gas from H_2 to biogas is similar for the cells with the $CeO_{2-\delta}$ and $Ce_{0.8}Fe_{0.2}O_{2-\delta}$ functional layers. The graph shows that the highest current density, equal to 0.339 A/cm^2, is achieved by fuel cells with undoped and Fe-doped ceria layers. However, in the latter case the larger fluctuations of current density vs. time are also observed. The reference sample as well as Mn and Fe containing cells show a similar rate of current density decrease in biogas, what means that the dynamics of the degradation process should be similar. In the case of catalytic layers with Co and Ni-doped ceria the current density drop after a gas change from hydrogen to biogas is larger than for the previously discussed cells. However, when these fuel cells are operating in the synthetic biogas, no major changes of current density were observed in a long run. The cell with $Ce_{0.8}Cu_{0.2}O_{2-\delta}$ layer shows an increase of current density at the initial stage of operation with biogas. However, after about 10 h of working, the catalyst is becoming deactivated, most probably due to a carbon deposition on the surface and a current density starts to decrease monotonically. Differences in the current density during the operation of the fuel cells in hydrogen can be explained on the basis of the microstructure of the layers. In the case of Co-, Ni- and Cu-doped materials, the porosity is much lower than in other layers. It can lead to slower diffusion of the gas fuel to the triple phase boundary. Moreover, if an absolute concentration of hydrogen at the anodic side of fuel cell is quite low, then the achieved absolute current density also tends to be lower. Therefore the analysis of composition of particular outlet gases is necessary to better understand these observations.

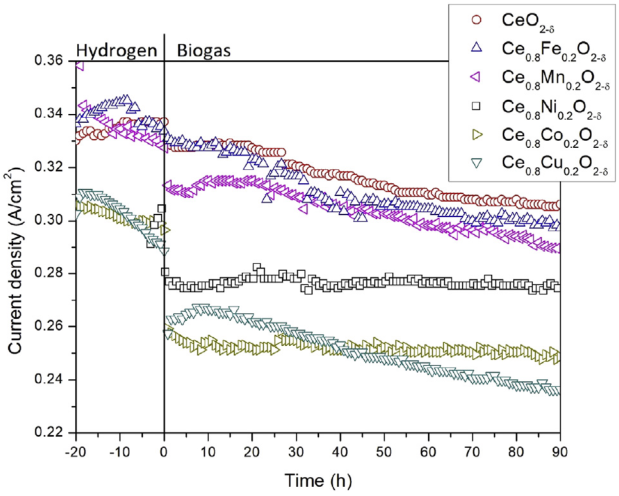

Fig. 4 – Plots for current density as a function of time for the fuel cells with the layers of undoped $CeO_{2-\delta}$ and $Ce_{0.8}A_{0.2}O_{2-\delta}$ (where A = Mn, Fe, Co, Ni, Cu).

Concentrations of the outlet gases. Changes in microstructure and phase composition

Changes in a composition of the outlet gases, for each of modified by additional layer cells, have been depicted in Fig. 5 and Fig. 6 simultaneously with calculated parameters describing catalytic activity and overall performance. The initial volume ratio of CH_4 to CO_2 in the supplied biogas was around 3:2 in order to simulate a biogas composition.

As it can be seen in Fig. 5 (left) and Fig. 6 (left) main constituent of outlet gases compositions strongly depends on the deposited layer type. For pure $CeO_{2-\delta}$ as well as for Mn- and Fe-doped ceria, hydrogen was detected as a gas with the highest concentration for almost whole investigation time. For fuel cells with Ni-, Co- and Cu-doped ceria layer methane dominated in the exhaust gases mixture. Higher concentrations of hydrogen in exhaust gases prove better catalytic activity of Mn- and Fe-doped ceria as well as pure $CeO_{2-\delta}$. At the same time lower amount of hydrogen and higher concentration of CH_4 in outlet mixture for $Ce_{0.8}Ni_{0.2}O_{2-\delta}$ stands for better utilization of obtained hydrogen via oxidation, what can be seen as higher current density compared to e.g., $Ce_{0.8}Co_{0.2}O_{2-\delta}$. Mentioned observations correspond well with electrical performance of investigated fuel cells (Fig. 4).

Time-dependent change of parameters describing performance of each of fuel cells (Fig. 5 right) can be divided by similarity into two groups. Analogous behavior of those can be observed for pure ceria layer as well as Mn- and Fe-doped. Conversion of CH_4 oscillates around value of 50% and decreases within operating time. Lower drop of conversion rate for both methane and carbon dioxide was noticed for Mn and Fe-doped ceria layers, what stands for better catalytic properties of prepared materials towards biogas reforming. Other parameters seem to be located within similar values.

Moving on to other three layers, big differences in all parameters are visible (Fig. 6 right). Nickel containing ceria revealed the highest H_2 selectivity. Although, mentioned layer had the worst methane conversion rate. In the end it results in slightly better efficiency, when it comes to fuel utilization and energy provision. What is more, for Cu- and Co-doped layers CO oxidation took place with higher rates than for Ni-doped ceria. It is clearly visible, that both Ni and Co containing layers were working with the highest stability, while Cu-doped showed the lowest performance over measuring time.

In order to facilitate comparison of the investigated layers, a graphic comparison of relative changes (in %) of current density and concentrations of individual outlet gases was made after 90 h of operation in biogas. Results are presented in Fig. 7. It shows that the lowest relative drop of current density found for Ni and Co-doped ceria is correlated with large decrease in H_2 and CO amount in outlet gases stream without such a big increase of unreacted fuel (CH_4 and CO_2). It means that H_2 and CO fuel is utilized effectively for electrochemical reactions (Eqs. (8) and (9)), giving stable electrical parameters.

What is more, different rates of decrease in catalytic activity towards biogas reforming for particular dopants can also

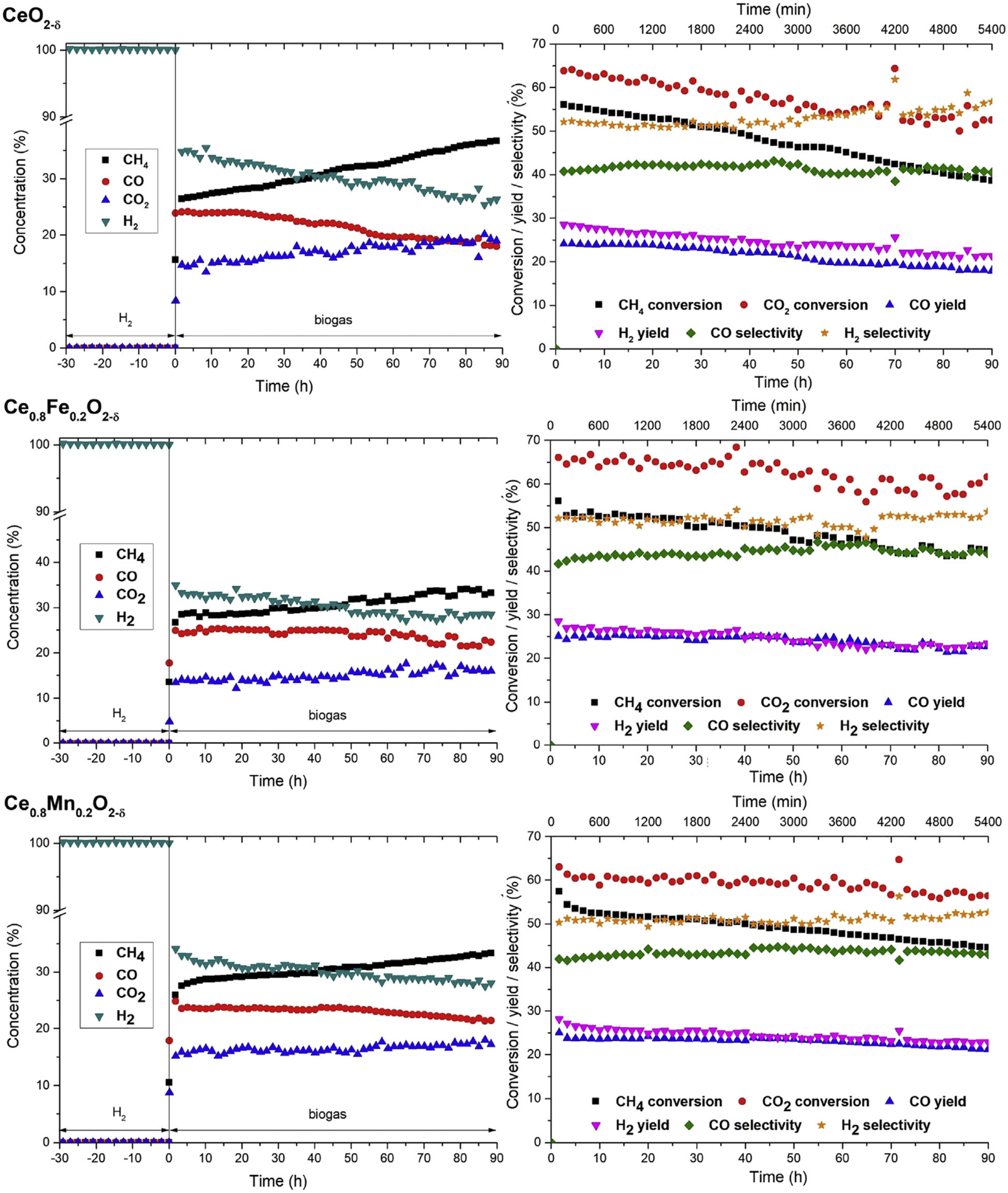

Fig. 5 – **Plots presenting (left) concentrations of exhaust gases vs. time for fuel cells with catalytic layers in the form of undoped $CeO_{2-\delta}$ and $Ce_{0.8}A_{0.2}O_{2-\delta}$ (where A = Fe, Mn) and (right) CH_4, CO_2 conversion rates, CO and H_2 selectivities/yields during operation in a synthetic biogas.**

originate from microstructural changes of layers as well as from a possible deposition of carbon. Additional XRD as well as SEM measurements have been done after operation in biogas in order to determine a phase composition of doped ceria layers, check possible diffusion of dopant ions into other structures and examine possible coke residuals. Both of mentioned factors are responsible for blocking active sites of catalytic material and thus hinder an internal reforming process. The results are presented in section Post-mortem analysis.

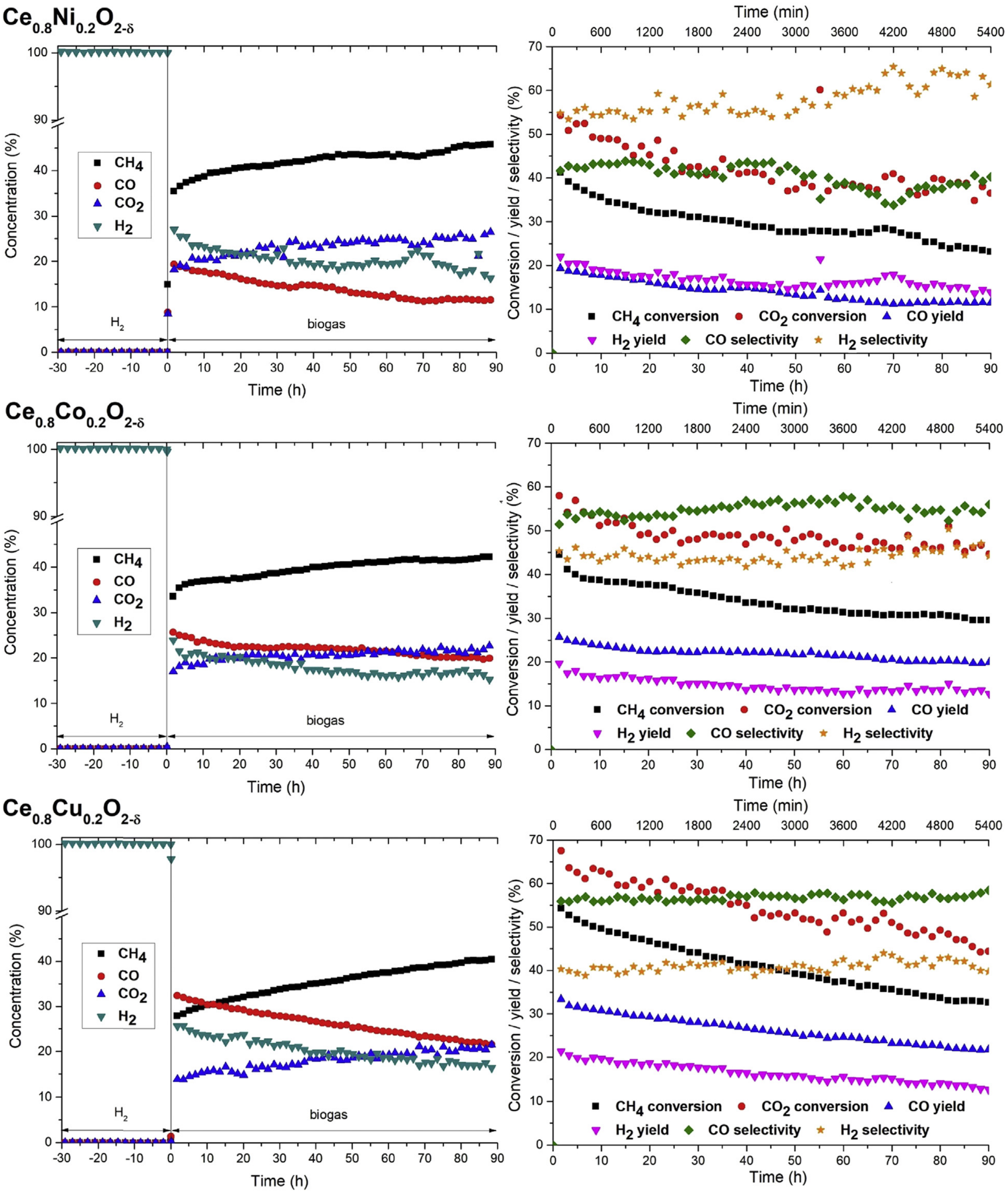

Fig. 6 – Plots presenting (left) concentrations of exhaust gases vs. time for fuel cells with catalytic layers in the form of $Ce_{0.8}A_{0.2}O_{2-\delta}$ (where A = Ni, Co, Cu) and (right) CH_4, CO_2 conversion rates, CO and H_2 selectivities/yields during operation in a synthetic biogas.

Chemical non-equilibrium analysis

Time-dependent values of reaction quotients Q_r calculated for a set of reactions presented in Eqs. (1)–(4) are shown in Fig. 8. It was found out that steam reforming reaction is fully shifted towards products during whole testing time for each of modified fuel cells. Mentioned result implies that steam assisted reforming of methane is strongly involved into hydrogen generation. An appearance of $Q_{r(t)}$ of steam reforming process for undoped, Mn- and Fe-doped ceria was found out to be very similar. That can be seen as a consistent behavior of reaction quotient change in time. For other layers,

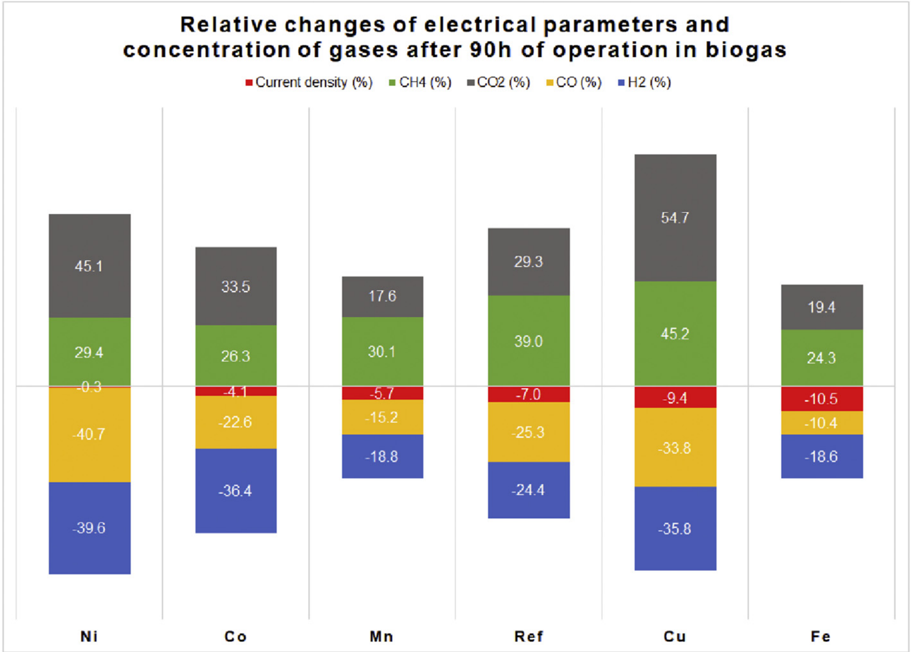

Fig. 7 – Comparison of relative changes of current density and concentrations of individual outlet gases (with respect to values in the beginning and in the end of operation in biogas) for SOFCs with $CeO_{2-\delta}$ (Ref) and with transition metal-doped ceria (Mn, Fe, Co, Ni, Cu).

being the subjects of this study, rapid change in Q_r value was observed. The same as for other types of considered reactions, rate of decrease or increase of quotients' values in time can illustrate how far from equilibrium point is each of reactions at given time. Indirectly, course of plotted function can deliver overall view on how efficiently different reactions are trying to reach their equilibrium points. The higher the change in calculated Q_r values through time, the bigger the difference between actual concentration of products and equilibrium composition. In that case reaction proceeds most probably slower and it's dominated by other reactions, which also aim to reach their equilibrium points. The same trend as in steam reforming reaction is also visible in dry reforming of methane. Considering both processes, it can be clearly seen, that layers consisting of $CeO_{2-\delta}$ without dopants and Mn/Fe additives are more active than Co-, Cu- and Ni-doped ones. This statement is also in agreement with exhaust gases concentrations measurement as well as electrical tests. While discussing RWGS (Eq. (3)) reaction, it is commonly assumed, that it operates with high rates near equilibrium within wide temperature range and can be omitted in order to simplify analysis of results [34]. However, in presented study values and time-changes of Q_r for RWGS reaction are similar. Furthermore, in order to involve RWGS process into hydrogen production and limit possible utilization of H_2 it should be shifted much more towards reactants (WGS). Methanation reaction for whole operating time is fully shifted towards reactants, mainly because of high temperature which strongly limit any exothermic reactions ($\Delta H = -165$ kJ/mol) and is considered to play a role rather in hydrogen formation.

Thermodynamical possibility of solid carbon formation was expressed by $\alpha_{C,r}$ coefficients (carbon activity coefficients) and presented in Fig. 9. As it can be seen, from reactions responsible for carbon accumulation (Eqs. (5)–(7)) only methane pyrolysis (Eq. (5)) carbon activity coefficient highly exceeds value of 1. It means that solid carbon species are favorable to form in existing atmosphere mostly due to that reaction. Two other processes are shifted to the reactants site, so most probably those help to remove carbon from anode's surface. Overall results of carbon activity coefficient calculations are in agreement with electrical measurements. For $CeO_{2-\delta}$, $Ce_{0.8}Mn_{0.2}O_{2-\delta}$, $Ce_{0.8}Fe_{0.2}O_{2-\delta}$ and $Ce_{0.8}Cu_{0.2}O_{2-\delta}$ changes of $\alpha_{C,r}$ parameter regarding methane pyrolysis reaction shows stable and rather fast process of coke production. It can be a major reason of constant drop in efficiency of those fuel cells (Fig. 4). SOFCs modified with additional layer of Ni- and Co-doped ceria shows significant stability within working time of the unit. It is most probably caused by slower carbon accumulation and slightly faster removal of deposits than in other examined samples. Plots of $\alpha_{C,r}$ for both of discussed layers shows that all of Eqs. (5)–(7) reactions responsible for coking more rapidly moves away from equilibrium states, what might stand for lower reaction rates. What is more, an addition of water into fueling stream and molecules generated after hydrogen oxidation shift both Bouduard (Eq. (6)) and CO reduction (Eq. (7)) reactions into direction, which promote carbon gasification. In fact, slightly smaller current density in fuel cells with Ni- and Co-doped ceria layers is compensated by better coking resistance. All the given statements can be also proved by carbon balance plots, depicting difference between inlet and outlet amount of carbon atoms (Fig. 10a and b). Carbon mass balance shows higher deposition rates for $CeO_{2-\delta}$, Mn- and Fe-doped ceria. For pure ceria layer drop in carbon accumulation is more rapid, what can explain better

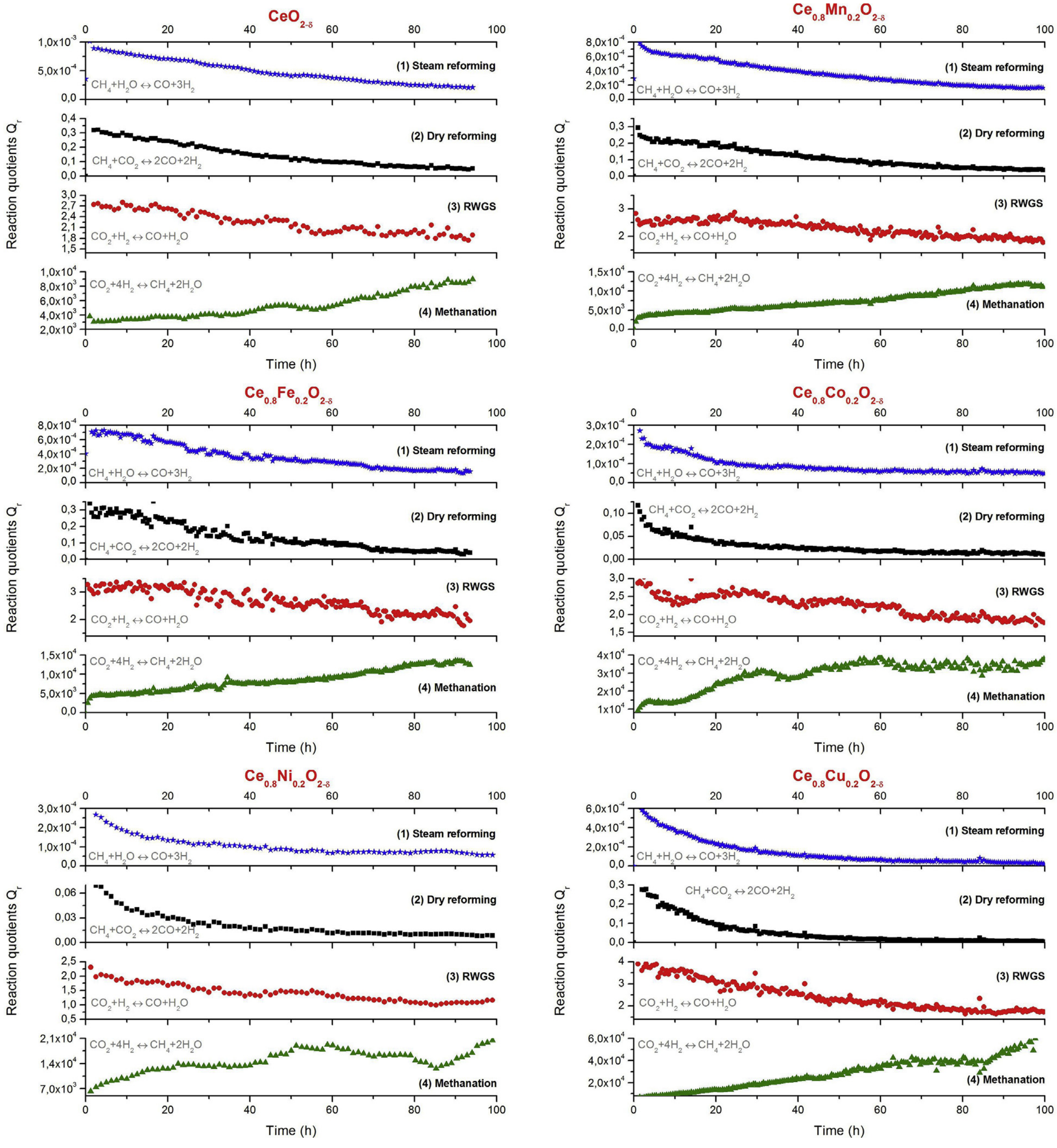

Fig. 8 – Time-dependent changes of Q_r (reaction quotient) for all mentioned reforming reactions.

performance in longer time. When it comes to Fe- and Mn-involving layers, $Ce_{0.8}Mn_{0.2}O_{2-\delta}$ shows slightly lower carbon balance, what in fact stabilize fuel cell work in a long run. For other three layers carbon balance values are around 30% lower, what results in slower carbon accumulation.

Considering whole collected data and analysis of the results, one should assume that steam reforming dominates over dry reforming and most probably strongly power-up hydrogen generation. At the same time H_2 is created via methane pyrolysis in high amounts, but also solid carbon species are being formed onto anode's surface. Other reactions have rather secondary role in hydrogen formation. The balance between processes, that create and consume hydrogen, as well as produce and remove carbon has a crucial meaning in overall performance of the final product.

Post-mortem analysis

The samples after operating in biogas have undergone XRD analysis in order to determine the phase composition of the anode with additional catalytic layer. The XRD patterns are shown in Fig. 11. It is clearly visible, that most of the samples

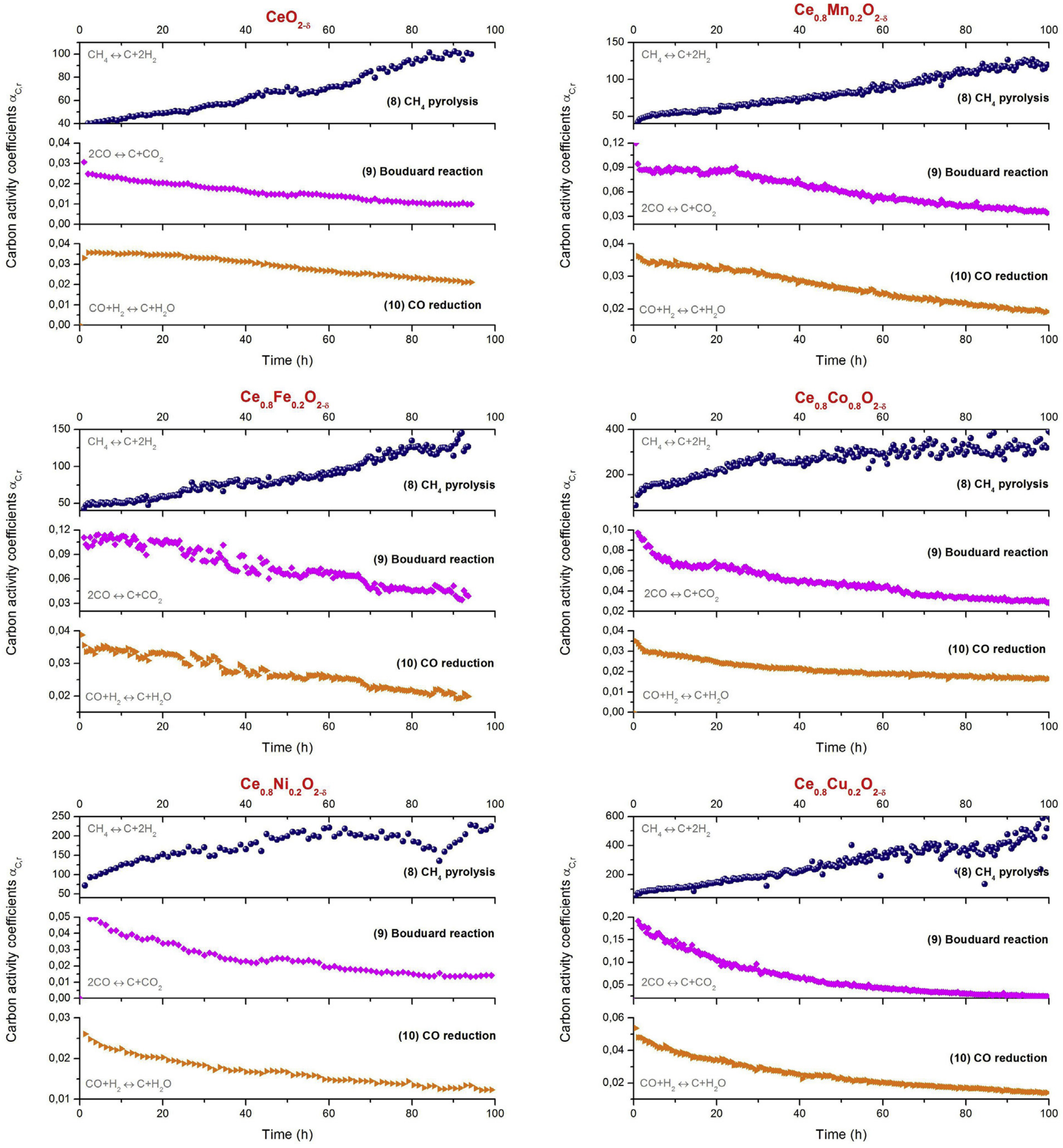

Fig. 9 – Carbon activity coefficients calculated for reactions responsible for carbon deposition.

do not show formation of any additional phases, different from CeO2 and Ni/YSZ derived from the catalytic layer and the cermet material, respectively. Additional phases can be observed for samples, in which the dopant was Mn or Co. Namely, phases of Ni_2Zr_3 and MnO can be observed for $Ce_{0.8}Mn_{0.2}O_{2-\delta}$, while YCeZr ($Y_{0.92}Ce_{0.04}Zr_{0.04}O_2$), Co_3O_4 (also seen before operating in biogas), and $CeNi_2$ were found for Co-doped layer. Traces of a deposited carbon were also identified for $Ce_{0.8}Co_{0.2}O_{2-\delta}$ layer in a form of a molecular carbon (C) and cobalt carbide (CoC_x). For all samples, neither carbon nor other impurities were clearly noticed. It might be a result of cooling fuel cells in hydrogen atmosphere. Additional steam, which probably formed from hydrogen oxidation, could cause removal of carbon by gasification. Small amount of neutral cerium in the reference material was identified. In addition, the material with the iron dopant shows a much lower value of CeO_2 signal intensity than the others. This is due to a large exfoliation of mentioned catalytic layer, what limited its intensity while XRD measurement. All additional phases, that appeared, most probably lowered the overall performance of prepared fuel cells and suggests insufficient long-run chemical stability of synthesized materials.

The analysis by SEM and EDX of samples after operation in biogas was performed to evaluate changes in microstructure

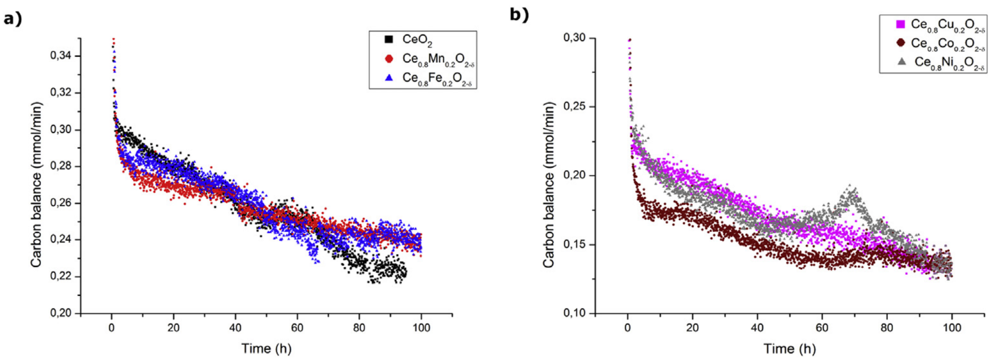

Fig. 10 – Carbon balance plots for a) pure CeO_2, Mn- and Fe-doped ceria; b) Cu-, Co- and Ni-doped ceria. Slower carbon accumulation for nickel, copper and cobalt can be observed.

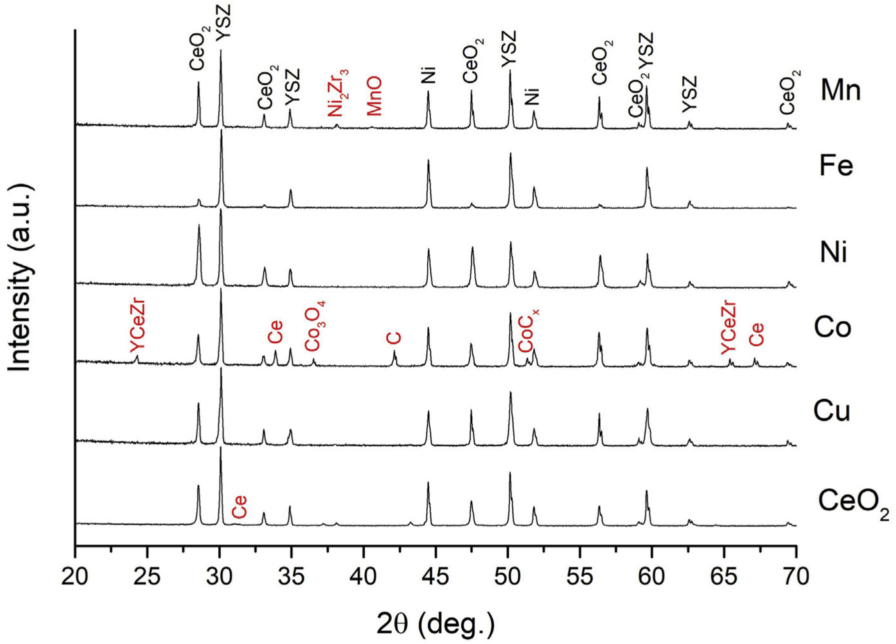

Fig. 11 – XRD patterns of $Ce_{0.8}A_{0.2}O_{2-\delta}$ (where A = Mn, Fe, Co, Ni, Cu) and $CeO_{2-\delta}$ after operation in biogas.

and to determine the percentage of atomic content of given elements in the material. The EDX measurement was performed linearly at a depth of 20 μm over the interface between the ceria-based catalytic layer and the Ni-YSZ anode support. Images of cross-sections for individual fuel cells are shown in Fig. 12 and the corresponding results of EDX measurements in Fig. 13. No measurements were made for samples with iron and copper dopants in the catalytic layer due to high damage of these layers during operation in biogas. Cracks and a high porosity of the catalytic layers are visible, while the structure of the cermet remains unchanged. In addition, there were no signs of accumulated carbon found. That was most probably due to the fact that fuel cell was cooled down in hydrogen atmosphere, not in biogas. EDX measurements indicated a penetration of the cerium ions at small depth to the Ni-YSZ cermet anode. For all samples, diffusion of Zr and Ni into the catalytic layer was also observed. It was found out that all dopants are present only in the catalytic layer and their concentration decreased to 0 close to the layer/anode interface. No diffusion of examined ceria dopants was noticed. Nickel signals were difficult to separate from each other due to presence of Ni both in catalytic layer and used Ni/YSZ cermet electrode.

Post-mortem SEM images of the catalytic layers' surfaces after testing in biogas atmosphere are presented in Fig. 14. A layer of $Ce_{0.8}Fe_{0.2}O_{2-\delta}$, that has been damaged during test, is not included. For catalytic of Mn-, Co- and Ni-doped ceria, the nanograins and the agglomerates are observed. Nickel containing layer revealed high tendency towards agglomeration of grains into bigger structures. Moreover, the high porosity is visible. For the catalytic material $Ce_{0.8}Cu_{0.2}O_{2-\delta}$ mainly large agglomerates connecting to each other can be observed. High growth of grains was noticed for Cu-doped ceria. What is more, porosity is visible, but surely smaller than for other layers. This can be a reason why mentioned material has shown poorer catalytic activity and lower performance of

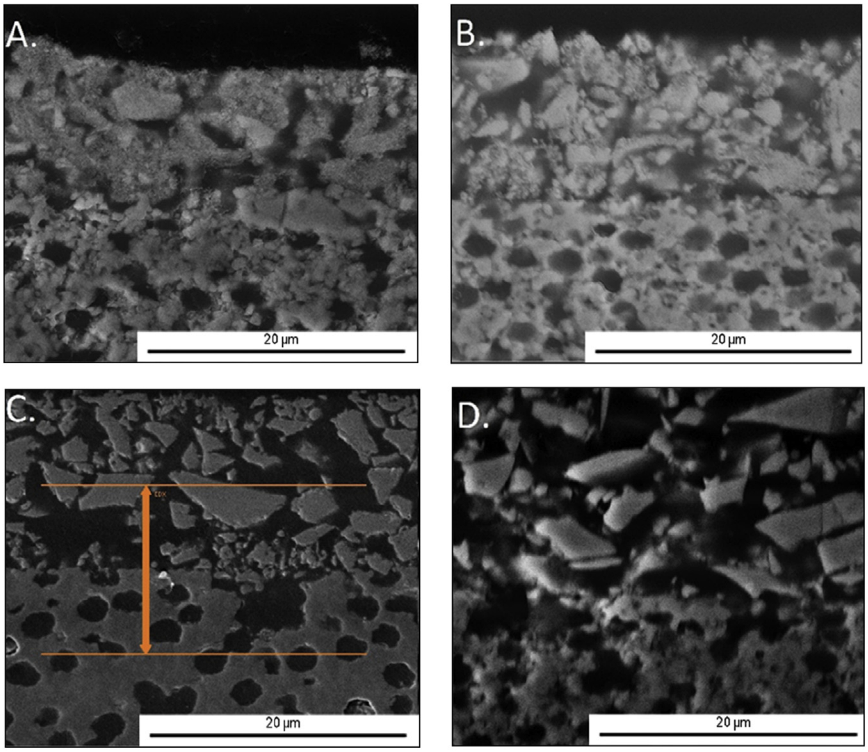

Fig. 12 – SEM micrographs of polished cross-sections of catalytic layers deposited on the anode support after operation in biogas. Catalytic layer CeO_2 (A) and $Ce_{0.8}A_{0.2}O_{2-\delta}$ (doped with Mn (B), Co (C), Ni (D)) are presented. Arrow indicating the range of the EDX measurement is included in C.

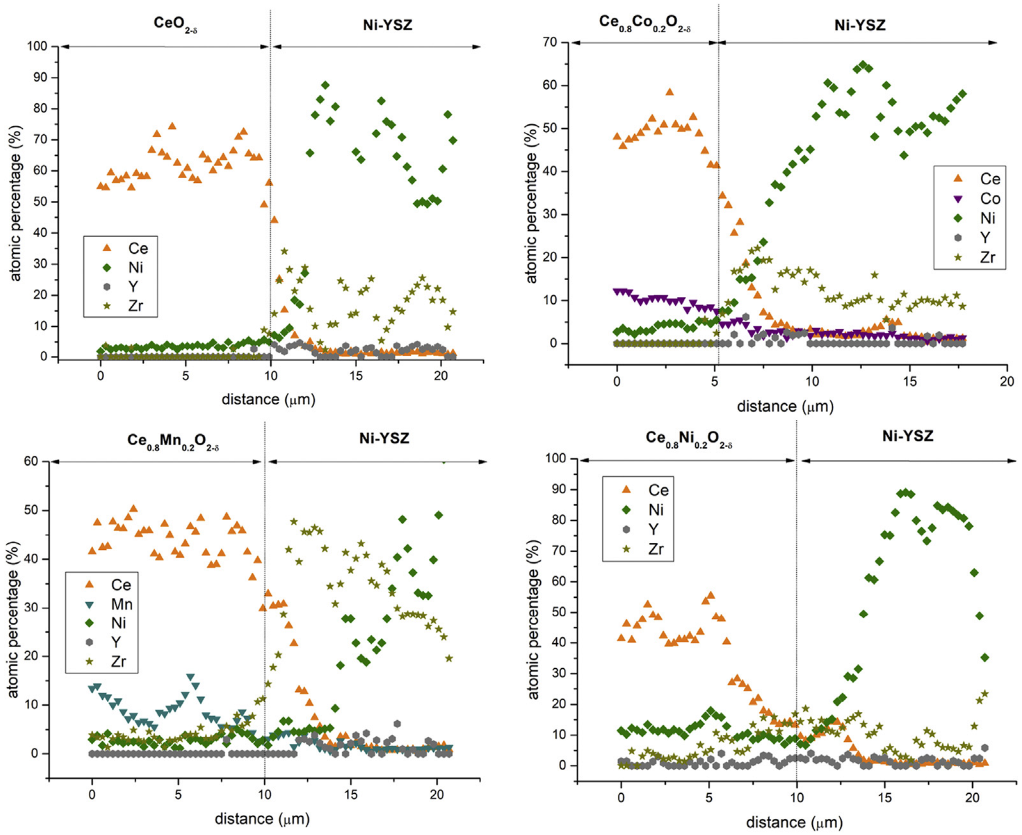

Fig. 13 – Linear EDX measurement results. Atomic percentage of individual elements in both catalytic layer and anode support are presented.

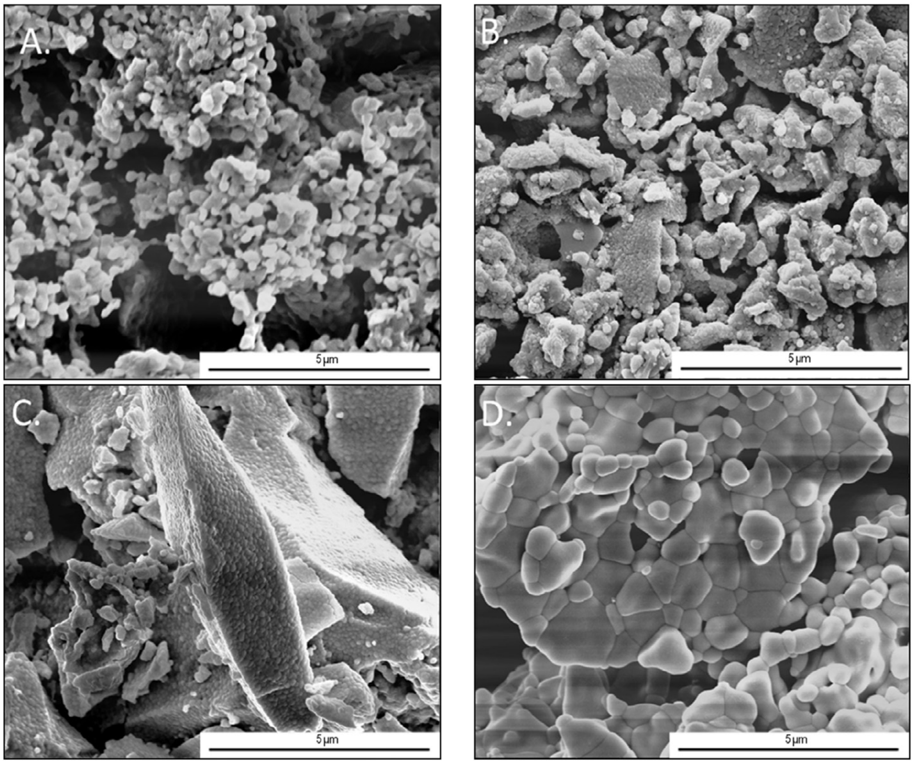

Fig. 14 – SEM micrographs of the surfaces of catalytic layers deposited on the SOFC anode after biogas tests: $Ce_{0.8}A_{0.2}O_{2-\delta}$ (doped with Mn (A), Co (B), Ni (C) and Cu (D)).

whole fuel cell. As mentioned before, carbon deposits are not clearly visible most probably due to cooling down of the fuel cells in hydrogen flux.

Conclusions

The purpose of this research was to analyze cerium oxides doped with elements from the group of transition metals as a catalytic layer for SOFC's anodes operating in biogas atmosphere. The general stoichiometry of the studied oxides was $Ce_{0.8}A_{0.2}O_{2-\delta}$ (where A = Mn, Fe, Co, Ni, Cu). All of the samples were synthesized by the reverse microemulsion method, which in most cases allowed obtaining nanocrystalline and pure, single-phase powders.

After performing electrical tests, a decrease of current density for all fuel cells except for those with Ni- and Co-doped ceria was observed. In addition, all fuel cells with doped-ceria layers have shown lower current density compared to the reference undoped cerium oxide layer.

Composition of outlet gases changed for each of examined catalytic layers. A dominant exhaust gas for Co-, Cu– and Ni-doped ceria catalytic layers was CH_4, whereas for undoped $CeO_{2-\delta}$ and both Mn and Fe-doped - hydrogen. This can be attributed to the catalytic activity of prepared functional layers, which corresponds also to change in overall reforming process. Chemical analysis derived from measured concentrations revealed that steam reforming and methane pyrolysis in all cases are more likely to be dominating processes. Other reaction are meant to have secondary role in hydrogen formation. At the same time delicate differences in reaction kinetics have significant influence on overall performance. Carbon deposition is mostly caused by methane pyrolysis due to low activation energy of this process. Addition of water into atmosphere increases possibility of carbon gasification.

Acknowledgements

This work was supported by the National Science Center under the grant No. NCN 2017/26/D/ST8/00822.

REFERENCES

[1] Stambouli AB, Traversa E. Solid oxide fuel cells (SOFCs): a review of an environmentally clean and efficient source of energy. Renew Sustain Energy Rev 2002;6:433–55. https://doi.org/10.1016/S1364-0321(02)00014-X.

[2] Van Herle J, Membrez Y, Bucheli O. Biogas as a fuel source for SOFC co-generators. J Power Sources 2004;127:300–12. https://doi.org/10.1016/j.jpowsour.2003.09.027.

[3] Shiratori Y, Oshima T, Sasaki K. Feasibility of direct-biogas SOFC. Int J Hydrogen Energy 2008;33:6316–21. https://doi.org/10.1016/j.ijhydene.2008.07.101.

[4] Shiratori Y, Ijichi T, Oshima T, Sasaki K. Internal reforming SOFC running on biogas. Int J Hydrogen Energy 2010;35:7905–12. https://doi.org/10.1016/j.ijhydene.2010.05.064.

[5] Trembly JP, Marquez AI, Ohrn TR, Bayless DJ. Effects of coal syngas and H_2S on the performance of solid oxide fuel cells: single-cell tests. J Power Sources 2006;158:263–73. https://doi.org/10.1016/j.jpowsour.2005.09.055.

[6] Kuchonthara P, Bhattacharya S, Tsutsumia A. Combination of thermochemical recuperative coal gasification cycle and fuel cell for power generation. Fuel 2005;84:1019–21. https://doi.org/10.1016/j.fuel.2004.08.024.

[7] Cayan NF, Zhi M, Pakalapati SR, Celik I, Wu N, Gemmen R. Effects of coal syngas impurities on anodes of solid oxide fuel cells. J Power Sources 2008;185:595–602. https://doi.org/10.1016/j.jpowsour.2008.06.058.

[8] Weiland P. Biogas production: current state and perspectives. Appl Microbiol Biotechnol 2010;85:849–60. https://doi.org/10.1007/s00253-009-2246-7.

[9] Szymczewska D, Karczewski J, Bochentyn B, Chrzan A, Gazda M, Jasiński P. Investigation of catalytic layers on anode for solid oxide fuel cells operating with synthetic biogas. Solid State Ionics 2015;271:109–15. https://doi.org/10.1016/j.ssi.2014.10.023.

[10] Haga K, Adachi S, Itoh K, Sasaki K. Poisoning of SOFC anodes by various fuel impurities. Solid State Ionics 2008;179:1427–31. https://doi.org/10.1016/j.ssi.2008.02.062.

[11] Cheng Z, Zha S, Liu M. Influence of cell voltage and current on sulfur poisoning behavior of solid oxide fuel cells. J Power Sources 2007;172:688–93. https://doi.org/10.1016/j.jpowsour.2007.07.052.

[12] Mogensen M, Primdahl S, Jorgensen MJ, Bagger C. Composite electrodes in solid oxide fuel cells and similar solid state devices. J Electroceram 2000;5:141–252. https://doi.org/10.1023/A:1009910202330.

[13] Chen T, Wang WG, Miao H, Tingshuai Li T, Xu C. Evaluation of carbon deposition behavior on the nickel/yttrium-stabilized zirconia anode-supported fuel cell fueled with simulated syngas. J Power Sources 2011;196:2461–8. https://doi.org/10.1016/j.jpowsour.2010.11.095.

[14] Finnerty CM, Coe NJ, Cunningham RH, Ormerod RM. SOFC system with integrated catalytic fuel processing. Catal Today 1998;46:137–45. https://doi.org/10.1016/S0378-7753(99)00496-6.

[15] Ozgur C, Dincer I, Hamdullahpur F. Effect of recirculation on carbon deposition for direct internal reforming solid oxide fuel cells. 3rd International Energy, Exergy and Environment Symposium; 2007.

[16] Singh D, Hernandez-Pacheco E, Hutton PN, Patel N, Mann MD. Carbon deposition in an SOFC fueled by tar-laden biomass gas: a thermodynamic analysis. J Power Sources 2005;142:194–9. https://doi.org/10.1016/j.jpowsour.2004.10.024.

[17] Sasaki K, Teraoka Y. Equilibria in fuel cell gases I. Equilibrium composition and reforming conditions. J Electrochem Soc 2003;150(7):A878–84. https://doi.org/10.1149/1.1577337.

[18] Karczewski J, Riegel B, Gazda M, Jasinski P, Kusz B. Electrical and structural properties of Nb-doped $SrTiO_3$. J Electroceram 2010;24:326–30. https://doi.org/10.1007/s10832-009-9578-7.

[19] Bochentyn B, Karczewski J, Molin S, Klimczuk T, Gazda M, Jasinski P, Safarik DJ, Kusz B. The comparisonof $SrTi_{0.98}Nb_{0.02}O_{3-\delta}$-$CeO_2$ and $SrTi_{0.98}Nb_{0.02}O_{3-\delta}$-YSZ composites for use in SOFC anodes. J Electroceram 2012;28:132–8. https://doi.org/10.1007/s10832-012-9693-8.

[20] Karczewski J, Bochentyn B, Molin S, Gazda M, Jasinski P, Kusz B. Solid oxide fuel cells with Ni infiltrated perovskite anode. Solid State Ionics 2012;221:11–4. https://doi.org/10.1016/j.ssi.2012.06.002.

[21] Bochentyn B, Karczewski J, Miruszewski T, Krupa A, Gazda M, Jasinski P, Kusz B. Donor-substituted $SrTi_{1+x}O_{3-\delta}$ anodes for SOFC. Solid State Ionics 2012;225:118–23. https://doi.org/10.1016/j.ssi.2012.05.015.

[22] Bochentyn B, Karczewski J, Gazda M, Jasinski P, Kusz B. Interactions between components of $SrTi_{0.98}Nb_{0.02}O_{3-\delta}$-YSZ and $SrTi_{0.98}Nb_{0.02}O_{3-\delta}$-$CeO_2$ composites. Phys Status Solidi 2013;210:538–45. https://doi.org/10.1002/pssa.201228380.

[23] Chlipała M, Błaszczak P, Wang SF, Jasiński P, Bochentyn B. In situ study of a composition of outlet gases from biogas fuelled Solid Oxide Fuel Cell performed by the Fourier Transform Infrared Spectroscopy. Int J Hydrogen Energy 2019;44:13864–74. https://doi.org/10.1016/j.ijhydene.2019.03.243.

[24] Wang SF, Wang YR, Yeh CT, Hsu YF, Chyou SD, Lee WT. Effects of bi-layer LSCF-based cathodes on characteristics of intermediate temperature SOFCs. J Power Sources 2011;196:977–87. https://doi.org/10.1016/j.jpowsour.2010.08.064.

[25] Zhao L, Hyodo J, Ishihara T, Sasaki K, Bishop SR. XRD and Raman spectroscopy study of Mn solubility in cerium oxide. ECS Transactions 2013;57:1607–12. https://doi.org/10.1149/05701.1607ecst.

[26] Laguna OH, Centeno MA, Boutonnet M, Odrizola JA. Fe-doped ceria solids synthesized by the microemulsion method for CO oxidation reactions. Appl Catal B Environ 2011;106:621–9. https://doi.org/10.1016/j.apcatb.2011.06.025.

[27] Jud E, Zhang Z, Sigle W, Gauckler LJ. Microstructure of cobalt oxide doped sintered ceria solid solutions. J Electroceram 2006;16:191–7. https://doi.org/10.1007/s10832-006-6258-8.

[28] Datta P, Majewski P, Aldinger F. Synthesis and reactivity study of gadolinia doped ceria-nickel: a potential anode material for solid oxide fuel cell. J Alloys Compd 2008;455:454–60. https://doi.org/10.1016/j.jallcom.2007.01.143.

[29] Zimmer P, Tschöpe A, Birringer R. Temperature-programmed reaction spectroscopy of ceria- and Cu/Ceria-Supported oxide catalyst. J Catal 2002;205:339–45. https://doi.org/10.1006/jcat.2001.3461.

[30] Bochentyn B, Chlipała M, Gazda M, Wang SF, Jasiński P. Copper and cobalt co-doped ceria as an anode catalyst for DIR-SOFCs fueled by biogas. Solid State Ionics 2019;330:47–53. https://doi.org/10.1016/j.ssi.2018.12.007.

[31] Escudero MJ, Gomez de Parada I, Fuerte A. Performance evaluation of WNi-CeO_2 as anode in a solid oxide fuel cell fed by simulated biogas mixtures. Int J Hydrogen Energy 2015;40:11303–14.

[32] Escudero MJ, Serrano JL. Individual impact of several impurities on the performance of direct internal reforming biogas solid oxide fuel cell using W-Ni-CeO_2 as anode. Int J Hydrogen Energy 2019;44:20616–31.

[33] Fuerte A, Valenzuela RX, Escudero MJ. Role of dopants on ceria-based anodes for IT-SOFCs powered by hydrocarbon fuels. Univers J Electr Electron Eng 2017;5(3):45–55. https://doi.org/10.13189/ujeee.2017.050301.

[34] Barroso Quiroga MM, Castro Luna AE. Kinetic analysis of rate data for dry reforming of methane. Ind Eng Chem Res 2007;46:5265–70. https://doi.org/10.1021/ie061645w.